A modal view of oscillations in inhomogeneous compressible mhd

P. S. Cally and S. T. Maddison*

February 5, 1996

Abstract

The description of oscillations in inhomogeneous magnetohydrodynamic plasmas in terms of spatial Fourier modes is extended beyond the previous analyses of the incompressible case to a fully compressible plasma in a rigid box. Attention is focused upon the cusp and Alfvén continua and their interaction with a discrete fast-wave spectrum. The modal approach yields novel insights, as well as providing a convenient method of numerical solution.

1 Introduction

Resonant absorption of ideal magnetohydrodynamic (mhd) waves in inhomogeneous plasmas has been an important topic in solar physics for many years, particularly following the suggestion of Ionson (1978) that it may be the long-sought mechanism for heating coronal loops. It has also been discussed in various other space plasma contexts, such as sunspots (Hollweg 1988) and the Earth's magnetosphere (Wright 1992 and many earlier references therein).

The process of resonant absorption, and the related phenomenon of phase mixing, may occur in magnetofluids when there is a cross-field inhomogeneity. They are most simply seen in the cartesian case of an ideal mhd plasma characterized by equilibrium density $\rho_0(x)$, gas pressure $p_0(x)$, and unidirectional magnetic field $\mathbf{B} = B_0(x)\hat{\mathbf{e}}_\mathbf{z}$. The inhomogeneity is manifest in the x direction only. Equilibrium demands that total pressure be uniform:

$$\frac{d}{dx}\left(\frac{\rho_0 c^2}{\gamma} + \frac{\rho_0 a^2}{2}\right) = 0, \tag{1.1}$$

where $a^2 = B_0^2/\mu\rho_0$ and $c^2 = \gamma p_0/\rho_0$ are the squared Alfvén and sound speeds respectively, γ is the ratio of specific heats, and μ is the magnetic permeability. If linear modes with y, z, and t dependence of the form $\exp i(k_x x + k_y y - \omega t)$ are sought, we obtain an ordinary differential equation with singular points, and correspondingly singular solutions, at Alfvén

*Department of Mathematics, Monash University, Clayton, Victoria 3168, Australia

resonances $\omega^2 = a^2 k_z^2$ and at cusp resonances $\omega^2 = c_T^2 k_z^2$, where $c_T = ac/(a^2+c^2)^{1/2}$ is the cusp speed (see Cally 1984 for a local mathematical analysis of these "critical levels"). Any impinging wave with frequency in the range of the Alfvén continuum $(a_{\min}k_z, a_{\max}k_z)$ or cusp continuum $(c_{T\min}k_z, c_{T\max}k_z)$ will excite these resonances and be partially absorbed. Interestingly, this absorption occurs despite the absence of any dissipative mechanism in the system. It is due to an effectively irreversible cascade of energy to progressively finer spatial scales via the process of phase mixing (Rae and Roberts 1981; Rae 1982), whereby neighbouring field lines oscillate at slightly varying frequencies and eventually differ significantly in phase. In reality, energy in these small scales will ultimately be thermalized by non-ideal processes (e.g., viscosity and resistivity), but this is incidental. Even in the absence of a resonantly interacting wave, the singular points in the differential equation are crucial mathematically in giving rise to continuous spectra and phase mixing, though the effect in this case may not be localized.

Much of the analytic investigation of phase mixing and resonant absorption (e.g., Ionson 1978; Rae and Roberts 1981) has been carried out in the incompressible limit $c \to \infty$, often based on the Laplace-transform/Green's-function approach of Sedláček (1971) for the mathematically equivalent cold plasma. The governing equation for the x component of the displacement ξ_x is then greatly simplified:

$$\frac{\partial}{\partial x}\left[\left(\frac{\partial^2}{\partial t^2}+\omega_p^2(x)\right)\frac{\partial \xi_x}{\partial x}\right] - K^2\left(\frac{\partial^2}{\partial t^2}+\omega_p^2(x)\right)\xi_x = 0, \tag{1.2}$$

where $\omega_p(x) = a(x)k_z$ and $K^2 = k_y^2 + k_z^2$. The Alfvén singularity is apparent on making the identification $\partial/\partial t \leftrightarrow -i\omega$ in (1.2), and the cusp resonance has disappeared.

Of particular interest has been the phenomenon of the Alfvén surface wave, which propagates along a discontinuity in Alfvén speed ($a(x) = a_+$ if $x < 0$, $a(x) = a_-$ if $x > 0$) with frequency $\omega_S = [\frac{1}{2}(\omega_+^2 + \omega_-^2)]^{1/2}$, where $\omega_\pm = a_\pm k_z$. If the discontinuity is smoothed out slightly to form a steep inhomogeneity, a surface-wave-like disturbance still propagates, but slowly decays in time. It was shown by Cally and Sedláček (1992) that, for a reasonably general Alfvén speed profile, the decay proceeds as $e^{-\eta_d t}$, where

$$\eta_d = \frac{\pi K}{16}\frac{(\omega_+^2 - \omega_-^2)^2}{\omega_S}\left|\frac{d\omega_p^2}{dx}\right|_{x_S}^{-1} \tag{1.3}$$

depends on the steepness of the Alfvén speed profile at the point x_S at which the surface wave is resonant (i.e., at which $\omega_p(x_S) = \omega_S$). (Note that $\eta_d \to 0$ as the profile is steepened to a discontinuity, as expected.) We may interpret this exponential decay as resonant absorption of the surface wave, especially as it is found that energy concentrates about the resonant point as the evolution progresses.

However, if we wish to examine the situation in which an external wave impinges transversally on the inhomogeneity, the incompressible approximation is unsuitable because the only mode which propagates in the surrounding homogeneous plasma is the Alfvén wave, and its energy flux is exactly channelled along the field lines. This is one reason for wanting to treat the compressible mhd plasma case. Another is that the incompressible limit is actually a very poor approximation to the solar corona, where generally $a \gg c$.

Recently, a new modal or Galerkin approach to the incompressible problem has been developed (Cally 1991), in which ξ_x is expanded in a Sturm-Liouville series of basis functions which fit the prescribed boundary conditions. Besides proving computationally convenient, this method has yielded significant novel insights into the process of resonant absorption of the surface wave (Cally and Sedláček 1992), and of phase mixing in general, in particular how it may be viewed as a propagation process in mode number space (Cally and Sedláček 1994; see also Sedláček and Cally 1994). Although there have been many other numerical treatments of resonant absorption and phase mixing, these have generally employed finite difference (e.g. Steinolfson 1984) or finite element (e.g. Poedts, Goossens, and Kerner 1989) methods, based in physical space, which have missed the fundamental simplification afforded by the modal description[1].

Mann, Wright, and Cally (1995) have extended the Galerkin technique to treat a cold mhd plasma $c \to 0$ (not to be confused with the cold plasma discussed by Sedláček 1971), which is governed by

$$a^{-2}(x)\frac{\partial^2 \xi_x}{\partial t^2} + \left(k_z^2 - \frac{\partial^2}{\partial x^2}\right)\xi_x = ik_y\frac{\partial \xi_y}{\partial x}, \tag{1.4}$$

$$a^{-2}(x)\frac{\partial^2 \xi_y}{\partial t^2} + K^2\xi_x = ik_y\frac{\partial \xi_x}{\partial x}. \tag{1.5}$$

With the sound speed set to zero the cusp continuum has obviously vanished, but the Alfvén continuum remains, as does the possibility for fast magnetoacoustic modes to propagate across field lines, and potentially to carry energy to an Alfvénic resonant point. If $k_y = 0$, (1.4) and (1.5) obviously decouple, and the fast and Alfvén waves do not interact. On the other hand, if $k_y \neq 0$ the authors concluded that mode conversion is possible, and that the incident fast wave may "feed" the Alfvén resonance. This process was found to lead to a significant build-up of energy around the resonant surface when the fast wave frequency lay in the Alfvén continuum. (However, we shall choose to interpret this question of mode conversion rather differently — see §3.)

In this paper, we further extend the Galerkin approach to treat a fully compressible warm mhd plasma. Our main purpose in §2 shall be to set up the mathematical formalism, whilst §3 is devoted to a discussion of the normal modes and spectra, and illustration with numerical examples. In particular, we shall address the question of what proportion of the total energy is "absorbed" by the plasma. We conclude briefly in §4.

2 Basic mathematical development

Perturbing and linearizing about an equilibrium defined by $\rho_0(x)$, $p_0(x)$, and $\mathbf{B} = B_0(x)\hat{\mathbf{e}}_\mathbf{z}$ consistent with (1.1), and assuming a y and z dependence of the form $\exp i(k_y y + k_z z)$,

[1]However, this is not to say that these direct numerical approaches are not the most convenient for examining specific physical models. The Galerkin technique is quite complicated, or even infeasible, if the boundary conditions are not simple. It's main purpose is to illuminate general principles rather than be an all-purpose numerical workhorse.

the ideal (i.e. dissipationless) mhd equations yield

$$\rho_0\left(\frac{\partial^2}{\partial t^2}+a^2k_z^2\right)\xi_x = -\frac{\partial p_T}{\partial x}, \tag{2.1}$$

$$\rho_0\left(\frac{\partial^2}{\partial t^2}+a^2k_z^2\right)\xi_y = -ik_y p_T, \tag{2.2}$$

$$\frac{\partial^2\xi_z}{\partial t^2} = ik_z c^2\boldsymbol{\nabla\cdot\xi}, \tag{2.3}$$

where $\boldsymbol{\xi}$ is the displacement vector, $p_T=-\rho_0[(a^2+c^2)\boldsymbol{\nabla\cdot\xi}-ia^2k_z\xi_z]$ is the total pressure perturbation, and $\boldsymbol{\nabla\cdot\xi}=\partial\xi_x/\partial x+ik_y\xi_y+ik_z\xi_z$.

It is convenient to redefine the displacement components to eliminate the explicit appearance of complex numbers in the equations: $\xi=\xi_x$, $\eta=i\xi_y$, and $\zeta=i\xi_z$. The governing system of differential equations is then

$$\frac{\partial^2\xi}{\partial t^2} = -a^2k_z^2\xi-\frac{1}{\rho_0}\frac{\partial p_T}{\partial x}, \tag{2.4}$$

$$\frac{\partial^2\eta}{\partial t^2} = -a^2k_z^2\eta+\frac{k_y}{\rho_0}p_T, \tag{2.5}$$

$$\frac{\partial^2\zeta}{\partial t^2} = -c^2k_z\left(\frac{\partial\xi}{\partial x}+k_y\eta+k_z\zeta\right), \tag{2.6}$$

where

$$p_T=-\rho_0(a^2+c^2)\left(\frac{\partial\xi}{\partial x}+k_y\eta+k_z\zeta\right)+\rho_0a^2k_z\zeta \tag{2.7}$$

is the Eulerian total pressure perturbation.

A great variety of different types of equilibrium are of course possible. For example, we might assume that the magnetic field is uniform ($\rho_0a^2=$ constant), or that the plasma is isothermal ($c=$ constant), or that the density is uniform. In the interest of keeping this paper concise, we shall resist the temptation to retain complete generality and adopt the first of these. The reason for this choice is that it is appropriate to the solar active region corona, where individual loops are distinguished from their neighbours primarily by differences in temperature and density rather than magnetic field strength. However, we are not trying to model in detail any specific physical system, but rather to develop general insights, so the choice of equilibrium is not crucial. The reader should have little trouble in adjusting the method described below to accommodate different equilibria.

To simplify the mathematics, we shall be even more specific in our choice of equilibrium. We take $\rho a^2=\text{constant}=1$ (the choice of constant represents an arbitrary selection of units). Equation (1.1) then indicates that ρc^2 is also constant; we set $\rho c^2=\gamma\beta/2$, where $\beta=2\mu p_0/B_0^2$, the "plasma beta", is the ratio of gas to magnetic pressures. Furthermore, following Mann, Wright, and Cally (1995), we choose to place our gas in a rigid "box" $0\le x\le\pi$, and give it non-uniform density

$$\rho_0(x)=\frac{1}{a^2(x)}=A^2+B^2\cos x, \tag{2.8}$$

where $A^2 \geq B^2 > 0$. The box supports fast cavity modes, i.e, fast waves which bounce back-and-forth across it.

Cally (1991) examined oscillations in the incompressible mhd plasma as governed by (1.2). Two distinct scenarios were discussed. In the first, the plasma was confined in a rigid box, as we propose to do here. This has the virtue of simplicity, and yet it illustrates most of the interesting physics. In the second scenario, an "embedded inhomogeneity" is also discussed. In this case, a monotonic inhomogeneity in $a(x)$ is sandwiched between two semi-infinite 0 regions. This is quite easily done, as the matching conditions at the edges of the inhomogeneity take the form of simple boundary conditions, and a discrete Sturm-Liouville basis may be developed which is then used to expand the solution inside the inhomogeneity in a Galerkin series.[2] However, no such simple replacement of the homogeneous regions by boundary conditions is possible in the compressible case, which is why we must content ourselves with the more restricted problem here.

Applying the rigid boundary conditions $\xi(0,t) = \xi(\pi,t) = 0$, we expand the x component of displacement in a Fourier sine series,

$$\xi(x,t) = \sum_{m=1}^{\infty} a_m(t) \sin mx. \tag{2.9}$$

The structure of the equations (2.4–2.6) suggests a cosine expansion for the other two components[3]:

$$\eta(x,t) = \frac{b_0(t)}{\sqrt{2}} + \sum_{m=1}^{\infty} b_m(t) \cos mx, \tag{2.10}$$

$$\zeta(x,t) = \frac{c_0(t)}{\sqrt{2}} + \sum_{m=1}^{\infty} c_m(t) \cos mx. \tag{2.11}$$

The expansions (2.9–2.11) together with the cosine profile (2.8) ensure that the large matrices with which we shall be working are banded. More general profiles may be treated at the expense of having to deal with full matrices.

Substituting (2.7) and (2.8) along with (2.9–2.11) into (2.4–2.6), an infinite system of constant coefficient linear ordinary differential equations results, which may be written most concisely in matrix form:

$$\mathbf{S}\ddot{\mathbf{X}} + \mathbf{Q}\mathbf{X} = \mathbf{0}\,. \tag{2.12}$$

Here $\mathbf{X} = (\mathbf{X}_0, \mathbf{X}_1, \mathbf{X}_2, \ldots)^T = (b_0, c_0, a_1, b_1, c_1, \ldots)^T$, where $\mathbf{X}_0 = (b_0, c_0)^T$ and $\mathbf{X}_m = (a_m, b_m, c_m)^T$ $(m = 1, 2, \ldots)$; $\mathbf{Q} = \mathrm{diag}[\mathbf{Q}_0, \mathbf{Q}_1, \mathbf{Q}_2, \ldots]$ where

$$\mathbf{Q}_0 = \begin{pmatrix} k_y^2 r + k_z^2 & \frac{1}{2}\gamma\beta k_y k_z \\ \frac{1}{2}\gamma\beta k_y k_z & \frac{1}{2}\gamma\beta k_z^2 \end{pmatrix}, \tag{2.13}$$

[2]The novel aspect of the embedded inhomogeneity is that it allows treatment of the surface wave; see the discussion in the introduction associated with (1.3).

[3]This expansion does not guarantee spectral accuracy — expansion in the eigenfunctions of a singular Sturm-Liouville system (e.g., Chebyshev polynomials) should be used for that — but this is a small price to pay for the greater simplicity (and banded matrices) afforded by the Fourier approach. See Cally and Sedláček (1994), §5, for a discussion of this point.

$$\mathbf{Q}_m = \begin{pmatrix} k_z^2 + m^2 r & k_y r m & \frac{1}{2}\gamma\beta k_z m \\ k_y r m & k_y^2 r + k_z^2 & \frac{1}{2}\gamma\beta k_y k_z \\ \frac{1}{2}\gamma\beta k_z m & \frac{1}{2}\gamma\beta k_y k_z & \frac{1}{2}\gamma\beta k_z^2 \end{pmatrix}, \qquad m = 1, 2, \ldots \tag{2.14}$$

and $r = 1 + \gamma\beta/2$; and

$$\mathbf{S} = \begin{pmatrix} A^2\mathbf{I}^{2\times 2} & \frac{1}{\sqrt{2}}B^2\mathbf{I}^{2\times 3} & & & \\ \frac{1}{\sqrt{2}}B^2\mathbf{I}^{3\times 2} & A^2\mathbf{I} & \frac{1}{2}B^2\mathbf{I} & & \\ & \frac{1}{2}B^2\mathbf{I} & A^2\mathbf{I} & \frac{1}{2}B^2\mathbf{I} & \\ & & \frac{1}{2}B^2\mathbf{I} & A^2\mathbf{I} & \ddots \\ & & & \ddots & \ddots \end{pmatrix} \tag{2.15}$$

where $\mathbf{I}$ represents the 3×3 identity matrix, $\mathbf{I}^{2\times 2}$ the 2×2 identity, and

$$\mathbf{I}^{3\times 2} = \begin{pmatrix} 0 & 0 \\ 1 & 0 \\ 0 & 1 \end{pmatrix}, \qquad \mathbf{I}^{2\times 3} = \begin{pmatrix} 0 & 1 & 0 \\ 0 & 0 & 1 \end{pmatrix} \tag{2.16}$$

Equation (2.12) may be formally solved by seeking a $\sin\omega t$ or $\cos\omega t$ time dependence, whence

$$\omega^2 \mathbf{S}\mathbf{X} = \mathbf{Q}\mathbf{X}\,. \tag{2.17}$$

Equation (2.17) is a generalized eigenvalue equation, and may be solved using commonly available numerical routines. However, we prefer to further reduce it to standard eigenvalue form

$$\mathbf{M}\mathbf{Y} = \omega^{-2}\mathbf{Y}\,, \tag{2.18}$$

where $\mathbf{Q} = \mathbf{R}^2$, $\mathbf{Y} = \mathbf{R}\mathbf{X}$, and $\mathbf{M} = \mathbf{R}^{-1}\mathbf{S}\mathbf{R}^{-1}$. Because it is symmetric block diagonal, it is a simple matter to take the square root of $\mathbf{Q}$ to yield $\mathbf{R}$.[4] Here ω^{-2} is the eigenvalue and $\mathbf{Y}$ the eigenvector. Obviously, $\mathbf{M}$ is real symmetric, and so the eigenvalues are real. Furthermore, it is positive definite[5], and so the eigenvalues are positive, and therefore the ω_n are all real. To solve (2.18), we use double precision LAPACK routines, making use of the symmetries and block structures of the matrices involved.

Having determined the eigenvalues and eigenvectors, we may express $\mathbf{Y}(t)$ in the form

$$Y_p(t) = \sum_{n=1}^{\infty} Z_{pn}\left(g_n \cos\omega_n t + \frac{h_n}{\omega_n}\sin\omega_n t\right) \tag{2.19}$$

[4]The procedure is as follows. By Theorem 8.1.1 of Golub and van Loan (1989), since the $\mathbf{Q}_m$ are real symmetric, we may write each $\mathbf{Q}_m = \mathbf{V}_m\mathbf{D}_m\mathbf{V}_m^T$, where $\mathbf{V}_m$ is the (orthogonal) fundamental matrix of $\mathbf{Q}_m$, and $\mathbf{D}_m$ is a diagonal matrix whose elements are its eigenvalues. It is easily verified that the $\mathbf{Q}_m$ are positive definite (the principal diagonal subdeterminants are all positive), and so the eigenvalues are positive. It is then easily verified that $\mathbf{R}_m = \mathbf{Q}_m^{1/2} = \mathbf{V}_m\mathbf{D}_m^{1/2}\mathbf{V}_m^T$, and thence $\mathbf{R} = \mathrm{diag}[\mathbf{R}_0, \mathbf{R}_1, \ldots]$. Furthermore, $\mathbf{R}^{-1} = \mathrm{diag}[\mathbf{R}_0^{-1}, \mathbf{R}_1^{-1}, \ldots]$. Since the $\mathbf{R}_m$ are at most 3×3, they are easily inverted directly.

[5]Write $\mathbf{M} = \tilde{\mathbf{R}}^{-1}\tilde{\mathbf{S}}\tilde{\mathbf{R}}^{-1}$, where $\tilde{\mathbf{R}}^{-1} = \mathrm{diag}[\sqrt{2}\mathbf{R}_0^{-1}, \mathbf{R_1}^{-1}, \mathbf{R}_2^{-1}, \ldots]$ and $\tilde{\mathbf{S}}$ is the same as $\mathbf{S}$ except that the $\{1,1\}$ entry is divided by 2 and the $\{1,2\}$ and $\{2,1\}$ entries by $\sqrt{2}$. Now, $\tilde{\mathbf{S}}$ is obviously positive definite, since it is diagonally dominant with all terms on the main diagonal being positive. The fact that $\mathbf{M}$ is positive definite then follows from Theorem 4.2.1 of Golub and van Loan (1989).

where $\mathbf{Z}$ is the fundamental matrix of $\mathbf{M}$, i.e., its columns are the normalized eigenvectors $\mathbf{Y}$ ordered by eigenvalue. $\mathbf{Z}$ is orthogonal, $\mathbf{Z}^T = \mathbf{Z}^{-1}$, from which it follows that the vectors $\mathbf{g}$ and $\mathbf{h}$ are given by

$$\mathbf{g} = \mathbf{Z}^T \mathbf{Y}|_{t=0} \tag{2.20}$$

$$\mathbf{h} = \mathbf{Z}^T \dot{\mathbf{Y}}|_{t=0}\,. \tag{2.21}$$

Finally, the coefficient vector $\mathbf{X}(t) = \mathbf{R}^{-1}\mathbf{Y}(t)$ may easily be constructed.

To sum up, we may determine the time evolution $(\xi(x,t), \eta(x,t), \zeta(x,t))$ of the system as follows:

1. Solve (2.18) for the eigenvalues ω^{-2} and fundamental matrix $\mathbf{Z}$. This need only be done once. Of course, in practice we truncate our modal expansions (2.9–2.11), $m \le N$. We therefore have $3N + 2$ eigenvalues and eigenvectors to deal with.

2. Equations (2.20–2.21) are solved (once) for $\mathbf{g}$ and $\mathbf{h}$.

3. For each time t of interest, $\mathbf{Y}(\mathrm{t})$ may be constructed using (2.19) — it will be accurate up until the time when energy cascades down to the finest scale considered, i.e., that associated with the mode $m = N$. Note that, as distinct from a finite difference or similar calculation, there is no need to step forward iteratively in time.

4. The coefficient matrix $\mathbf{X}(t) = \mathbf{R}^{-1}\mathbf{Y}(t)$ is then constructed at each t. Since $\mathbf{R}$ is block diagonal, $\mathbf{R}^{-1}$ is easily constructed once and for all at the start.

5. Finally, the displacements may be recovered from (2.9–2.11) for a range of x values.

However, graphs of $(\xi(x,t), \eta(x,t), \zeta(x,t))$ against x for fixed t, or against t for fixed x, are not particularly enlightening. Cally (1991), and particularly Cally and Sedláček(1994), preferred to focus on the propagation of energy in modenumber space, in other words, on the flow of energy between various spatial scales. This energy cascade to fine scales is the essence of phase mixing. The energy is easily identified within our matrix formalism. Premultiplying (2.12) by $\dot{\mathbf{X}}^T$ yields

$$\frac{d}{dt}\left(\dot{\mathbf{X}}^T \mathbf{S} \dot{\mathbf{X}} + \mathbf{X}^T \mathbf{Q} \mathbf{X}\right) = 0\,. \tag{2.22}$$

This invariant quantity is easily seen to be the total energy of the system,

$$E = \tfrac{1}{2}\left(\dot{\mathbf{X}}^T \mathbf{S} \dot{\mathbf{X}} + \mathbf{X}^T \mathbf{Q} \mathbf{X}\right) \tag{2.23}$$

$$= \tfrac{1}{2}\left(\dot{\mathbf{Y}}^T \mathbf{M} \dot{\mathbf{Y}} + \mathbf{Y}^T \mathbf{Y}\right) \tag{2.24}$$

$$= \tfrac{1}{2}\sum_{n=0}^{\infty}\left(\left(\frac{h_n}{\omega_n}\right)^2 + g_n^2\right)\,. \tag{2.25}$$

Furthermore, we may identify the energy associated with mode m as

$$E_m = \tfrac{1}{2}\left(\dot{\mathbf{X}}_m^T \mathbf{S}_{mm} \dot{\mathbf{X}}_m + \dot{\mathbf{X}}_m^T \mathbf{S}_{m\,m-1} \dot{\mathbf{X}}_{m-1} + \dot{\mathbf{X}}_m^T \mathbf{S}_{m\,m+1} \dot{\mathbf{X}}_{m+1} + \mathbf{X}_m^T \mathbf{Q}_m \mathbf{X}_m\right)\,, \tag{2.26}$$

where the $\mathbf{S}_{m\,m-1}$ etc are the blocks making up the block-tridiagonal matrix $\mathbf{S}$ as explicated in (2.15). The total energy is

$$E = \sum_{m=0}^{\infty} E_m\,. \tag{2.27}$$

In practice, we always normalize the total energy to unity.

3 Barston modes, spectra, and resonant absorption

In an early treatment of oscillations governed by (1.2), Barston (1964) showed that normal modes with frequencies lying within the Alfvén continuum exist only within the class of generalized functions. In particular, ξ_x must have a logarithmic singularity and a Heaviside step at the resonant point. Although this singular behaviour disappears on inverting the temporal and spatial Fourier transforms for general non-singular initial conditions, it nevertheless reduces the attractiveness of solution by expansion in normal modes. Cally (1991) subsequently showed that these *Barston modes* appear very naturally within the Galerkin description; we shall now see how to generalize this to the case of compressible mhd.

Defining $\mathbf{W} = \mathbf{R}^{-1}\mathbf{Z}$, (2.19) gives

$$X_p(t) = \sum_{n=1}^{\infty} W_{pn}\left(g_n \cos\omega_n t + \frac{h_n}{\omega_n}\sin\omega_n t\right)\,. \tag{3.1}$$

Combining this with (2.9) we have (noting that $a_m = X_{3m}$)

$$\begin{aligned}
\xi(x,t) &= \sum_{m=1}^{\infty}\sum_{n=1}^{\infty} W_{3m\,n}\left(g_n \cos\omega_n t + \frac{h_n}{\omega_n}\sin\omega_n t\right)\sin mx && (3.2)\\
&= \sum_{n=1}^{\infty}\left(g_n \cos\omega_n t + \frac{h_n}{\omega_n}\sin\omega_n t\right)\varphi_n^x(x) && (3.3)
\end{aligned}$$

where

$$\varphi_n^x(x) = \sum_{m=1}^{\infty} W_{3m\,n}\sin mx\,. \tag{3.4}$$

Equation (3.3) shows that $\xi(x,t)$ may be expanded in functions $\varphi_n^x(x)$, each of which oscillates at its own characteristic frequency ω_n. These are the Barston modes. The normal mode expansion method therefore is equivalent to our Fourier expansion — they are related simply by reversing the order of the two sums in (3.2). The Fourier method though has the advantage of requiring fewer terms in the series to obtain a given accuracy when expanding a non-singular function. The y and z components, φ_n^y and φ_n^z, of the Barston displacements may be determined similarly:

$$\begin{aligned}
\varphi_n^y(x) &= \frac{W_{1\,n}}{\sqrt{2}} + \sum_{m=1}^{\infty} W_{3m+1\,n}\cos mx && (3.5)\\
\varphi_n^z(x) &= \frac{W_{2\,n}}{\sqrt{2}} + \sum_{m=1}^{\infty} W_{3m+2\,n}\cos mx\,. && (3.6)
\end{aligned}$$

Finally, we note that the energy associated with each of the Barston modes may be read directly from (2.25):

$$\varepsilon_n = \tfrac{1}{2}\left(\left(\frac{h_n}{\omega_n}\right)^2 + g_n^2\right) . \tag{3.7}$$

As mentioned in the introduction, the system governed by (2.1– 2.3) possesses Alfvén and cusp continua as part of its spectrum. Due to the finite extent of the confining rigid box, there will also be a discrete fast-wave spectrum. How are these manifested in our modal approach, were our eigenspectrum is necessarily discrete (consisting of $3N+2$ poles if the modal expansion (2.9–2.11) is truncated to $m \le N$)? In the modal analysis of the incompressible mhd plasma (Cally 1991), where only an Alfvén continuum exists, it was found that the discrete eigenfrequencies ω_n, $n = 0, 1, \ldots, N$, all lie in the range $(a_{\min}k_z, a_{\max}k_z)$, and in fact become dense in that interval as $N \to \infty$. In this way, the continuous spectrum is mimicked. We find essentially the same thing here; the eigenspectrum is split into three parts, two of which yield the cusp and Alfvén continua as $N \to \infty$, whilst the third is discrete.

To illustrate these features, we focus on the following scenario: $a_{\min} = 1$, $a_{\max} = \sqrt{2}$, $\frac{1}{2}\gamma\beta = \frac{1}{3}$, $k_y = 1$, and $k_z = 1$, 3, and 10. The Alfvén continuum is therefore $1 < \omega/k_z < \sqrt{2}$, and the cusp continuum is $1/2 < \omega/k_z < 1/\sqrt{2}$. For ease of interpretation, the parameters have been chosen so that the two continua are disjoint. Four cases are considered: (a) $k_z = 1$, with $a_1(0) = 1$; (b) $k_z = 3$, with $a_1(0) = 1$; (c) $k_z = 10$, with $a_1(0) = 1$; and (d) $k_z = 10$, with $c_0(0) = 1$. In each case, all other $a_m(0)$, $b_m(0)$, $c_m(0)$, $\dot{a}_m(0)$, $\dot{b}_m(0)$, and $\dot{c}_m(0)$ are set to zero. These conditions correspond to setting large-scale initial displacements (in the x direction in cases (a–c), in the z direction in case (d)), with zero initial velocities. We use $N = 120$ throughout, so there are 121 Fourier modes and 362 eigenfrequencies.

Since we wish to explore the interaction of the fast waves with the continua, we would like to first estimate the discrete fast spectrum neglecting the effects of these continua. Presumably, interesting phenomena will result when this approximate fast spectrum overlaps the continua. We adopt a WKB approach, and neglect k_y and k_z in comparison to $\partial/\partial x$. This yields $\partial^2\xi/\partial t^2 \sim (a^2 + c^2)\partial^2\xi/\partial x^2$, which obviously retains no information about the continua. We may then estimate the fast spectrum using the lowest order WKB approximation (Bender and Orszag 1978, chap. 10), to find

$$\omega_\nu \sim \omega_{\rm WKB} = \frac{\nu\pi\sqrt{r}}{\int_0^\pi \sqrt{A^2 + B^2\cos x}\,dx} , \qquad \text{as } \nu \to \infty , \tag{3.8}$$

where $\nu = 1, 2, \ldots$. For the example being considered here, this is $\omega_\nu \sim 1.34291\nu$. Table 1 illustrates how this approximation improves with increasing harmonic degree and decreasing k_z, as expected. An important point to note here is that, whereas the minimum and maximum frequencies of the continua scale linearly with k_z, the eigenfrequencies of the discrete spectrum are independent of $\mathbf{k}$ at the lowest order of approximation. It is therefore possible to adjust k_z to engineer an overlap between the discrete WKB and continuous spectra. We shall make use of this in the examples discussed below.

Unlike in the incompressible case, the closely packed eigenfrequencies mimicking the continua do not necessarily lie strictly within the expected ranges $(a_{\min}k_z, a_{\max}k_z)$ or

ω_{WKB}	ω for $k_z = 1$	ω for $k_z = 3$	ω for $k_z = 10$
—	—	2.124*	7.098*
—	0.723*	2.148*	7.124*
—	1.782	2.308*	7.172*
1.343	2.301	4.313	7.257*
2.686	3.247	4.734	7.399*
4.029	4.422	5.593	7.633*
5.372	5.673	6.629	8.018*
6.715	6.958	7.759	14.163
8.057	8.261	8.948	14.609
9.400	9.576	10.175	15.374
10.743	10.897	11.428	16.225
12.086	12.223	12.699	17.146
13.429	13.552	13.983	18.122
⋮	⋮	⋮	⋮
107.433	107.449	107.504	108.131
⋮	⋮	⋮	⋮

Table 1: *The lowest few frequencies of the discrete spectrum compared with the WKB formula (3.8). Those frequencies marked with an asterisk lie in the gap between the cusp and Alfvén continua. The others lie above the Alfvén continuum.*

$(c_{T\mathrm{min}}k_z, c_{T\mathrm{max}}k_z)$, but sometimes spill over the edges by tiny amounts. Of course, this is rectified in the limit $N \to \infty$. Nevertheless, this behaviour suggests that we need a criterion for deciding if an eigenfrequency is associated with the continuous or discrete spectrum. One possibility is to recalculate the eigenspectrum of (2.18) with a different number N of modes. The discrete spectrum will remain unaltered (for harmonic degree much less than N), whilst eigenvalues in the continuous spectra will be changed significantly (approximately N eigenvalues are spread smoothly — though not evenly — across each of the continuous spectra). However, a more convenient approach is based on very different structures of the associated eigenvectors $\mathbf{X} = [x_1, x_2, \ldots, x_{3N+2}]^T$. Since, as mentioned in the introduction, the normal modes from the continuum are singular, whereas the discrete ones are not, it may be shown that the x_n oscillate with increasing n in the former case, whereas they decay rapidly in the latter case (see the discussion on pp 460–462 of Cally 1991). Each eigenvector is easily checked, and therefore its eigenvalue is readily classified as belonging to the continuous or discrete spectrum.

Now, the important point is this: the energy in each Barston mode, given by (3.7), is invariant in time. So, given a particular initial disturbance of large scale, we can easily calculate the energy resident in the continuum and that in the discrete spectrum. Normally[6], the former will propagate to arbitrarily fine scales, whilst the latter will persist

[6]Of course there are counterexamples. Most simply, if a single Barston mode from the continuum is excited, it remains invariant in form indefinitely, and so no phase mixing or resonant absorption takes

at large scale. The fraction of energy "absorbed" by the plasma is therefore simply that initially placed in the continuum.

We now illustrate these points graphically. Figures 1–4 show the energies ε_n in each of the Barston modes in the continua and low end of the discrete spectrum for the cases (a–d) introduced above. The rectangular boxes enclose the (exact) continua, cusp and Alfvén. Reference to figure 1 indicates that most (79.76%) of the energy is placed in the discrete fast-wave spectrum in case (a). This is to be expected in view of the WKB analysis summarized in Table 1, as only the lowest WKB mode overlaps the (Alfvén) continuum. With $k_z = 3$ (figure 2) however, the overlap is substantial, and 87.22% of the energy resides in the continuum. This effect is amplified in case (c) — figure 3 — where the higher density of points in the discrete spectrum yields several distinct peaks in the continuum energy. Finally, in figure 4, we see the effect of changing the polarization of the initial displacement to field-aligned, thereby preferentially exciting the slow rather than the Alfvén continuum.

Figures 5–8 display energy propagation diagrams corresponding to figures 1–4 respectively. These show the energies in each of the Fourier modes (see eqn. (2.26)) at a time where energy is nearing the smallest scale. The upper panel in each case displays the total energy, whilst the bottom panel shows only that associated with the continuum. Initially, at $t = 0$, all energy in both spectra is at low m but, as expected, and as shown here, the continuum energy propagates to high m, leaving none behind (though the tail in figure 7 is rather long and messy). On the other hand, energy in the discrete spectrum remains at low mode number.

Consider an inhomogeneous region of width L in which the continuum frequency $\omega_p(x)$, either cusp or Alfvén, varies monotonically, $\omega_- < \omega_p(x) < \omega_+$. As explained in §2 of Cally and Sedláček (1994), the speed of energy propagation in modenumber space of the energy cascade associated with this continuum is $\pi^{-1} L \max |\omega_p'(x)|$ modes per unit time. In our example, this is 0.219, 0.658, and 2.193 for $k_z = 1$, 3, and 10 respectively for the Alfvén continuum, and 1.097 for $k_z = 10$ for the cusp continuum. At the times corresponding to figures 5–8, i.e., $t = 400$, 125, 40, and 80, this suggests that the energy front should be at approximately modes 88, 82, 88, and 88 respectively. This is in excellent agreement with these figures. (Note the slight perturbation ahead of the front in figure 8. This is energy in the faster mixing Alfvén continuum.) Furthermore, the messy tail in figure 7 may now be understood. It is due to the multiple energy peaks in the Alfvén continuum of figure 3, each of which is largely confined to a subinterval, and each therefore has its own characteristic propagation speed.

Finally, let us look at the physical-space energy density (Zorzan 1989)

$$H(x,t) = \tfrac{1}{2}\rho_0(\dot{\xi}^2 + \dot{\eta}^2 + \dot{\zeta}^2) + \frac{r}{2}\left[\left(\frac{\partial \xi}{\partial x}\right)^2 + k_y\left(\eta\frac{\partial \xi}{\partial x} - \xi\frac{\partial \eta}{\partial x}\right)\right]$$

place. Indeed, even if a finite number of these Barston modes are initiated, the system will eventually return to its initial state if their frequencies are commensurable, or arbitrarily close to it if incommensurable. However, we take to be the normal situation that in which only an interval or intervals from the continua are excited — this is necessary if the initial perturbation is non-singular — in which case all continuum energy phase mixes to arbitrarily fine scales.

$$+\frac{\gamma\beta}{4}\left[k_z\left(\frac{\partial\xi}{\partial x}\zeta-\xi\frac{\partial\zeta}{\partial x}\right)+(k_y\eta+k_z\zeta)\right]+\tfrac{1}{2}\left[k_z^2\xi^2+\left(k_y^2+k_z^2\right)\eta^2\right]. \qquad (3.9)$$

For case (b), we see from figure 2 that the Alfvén continuum energy is strongly peaked around $\omega=3.7$, corresponding to $x=\cos^{-1}[(k_z^2\omega^{-2}-A^2)B^{-2}]\approx 1.95$. This is in excellent agreement with the location of the resonant peak in figure 9. We may choose to interpret this as evidence of resonant absorption of a fast wave (cf. Mann, Wright, and Cally 1995), though within the formalism we have developed in this paper the peak in the energy in the Alfvén continuum would not be classed as a fast wave. The five energy peaks in the Alfvén continuum evident in figure 7 similarly each give rise to a resonant peak in H (not shown).

4 Conclusions

The modal approach to mhd phase mixing and resonant absorption has been partly extended from the incompressible to compressible cases. At least for the system in a box considered here, it provides a convenient numerical framework for calculating the evolution of the system to high precision (certainly far more practical than the Laplace transform approach). More important though is the novel pedagogical context afforded by this description in terms of spatial Fourier expansions. Questions of some complexity when viewed from the Laplace transform/Green's function formalism become almost trivial in the new system. In particular, it is a simple matter, given initial conditions, to determine how much energy lies in the continua, and this will normally be precisely the amount lost from the large scale due to phase mixing.

Resonant absorption and phase mixing are sometimes thought of as different phenomena. However, within our modal framework, they are seen to be the same thing. We do not think of the discrete fast spectrum somehow interacting with the continua and losing energy to them. Rather, each is totally independent. The continuum energy though may show distinct peaks at certain frequencies roughly consistent with where a fast mode might have been expected if not for the continua. These peaks in frequency space lead to a build up of resonant peaks in physical space, as explained at the end of §3, by the process of phase mixing.

ACKNOWLEDGEMENT

The authors wish to thank the Australian Research Council for funding this project.

REFERENCES

Barston, E. M. 1964 Electrostatic oscillations in inhomogeneous cold plasmas. *Ann. Phys. (N. Y.)* **29**, 282–303.

Bender, C. M. and Orszag, S. A. 1978 *Advanced Mathematical Methods for Scientists and Engineers.* McGraw-Hill.

Cally, P. S. 1984 Magnetohydrodynamic critical levels and radiative damping. *Astron. Astrophys.* **136**, 121–126.

Cally, P. S. 1991 Phase-mixing and surface waves: a new interpretation. *J. Plasma Phys.* **45**, 453–479.

Cally, P. S. and Sedláček, Z. 1992 Phase mixing and surface-wave decay in an inhomogeneous plasma. *J. Plasma Phys.* **48**, 145–158.

Cally, P. S. and Sedláček, Z. 1994 A Fourier-space description of oscillations in an inhomogeneous plasma. Part 2. Discrete approach. *J. Plasma Phys.* **52**, 265–296.

Golub, G. H. and van Loan, C. F. 1989 *Matrix Computations,* 2nd edition. Johns Hopkins University Press.

Ionson, J. A. 1978 Resonant absorption of Alfvénic surface waves and the heating of solar coronal loops. *Astrophys. J.* **226**, 650-673.

Mann, I. R., Wright, A. N., and Cally, P. S. 1995 Coupling of magnetospheric cavity modes to field line resonances: a study of resonance widths. *JGR* **100**, 19441–19456.

Poedts, S., Goossens, M., and Kerner, W. 1989 Numerical simulation of coronal heating by resonant absorption of Alfvén waves. *Solar Phys.* **123**, 83–115.

Rae, I. C. 1982 Resonant absorption and the electrostatic oscillations of a cold inhomogeneous plasma. *Plasma Physics* **24**, 133.

Rae, I. C. and Roberts, B. 1981 Surface waves and the heating of the corona. *Geophys. Astrophys. Fluid Dynamics* **18**, 197–226.

Sedláček, Z. 1971 Electrostatic oscillations in cold inhomogeneous plasma. I. Differential equation approach. *J. Plasma Phys.* **5**, 239–263.

Sedláček, Z. and Cally, P. S. 1994 A Fourier-space description of oscillations in an inhomogeneous plasma. Part 1. Continuous Fourier transformation. *J. Plasma Phys.* **52**, 245–264.

Steinolfson, R. S. 1984 Resonant absorption of phase-mixed Alfvén surface waves in ideal and resistive magnetohydrodynamics: initial-value problem. *Phys. Fluids* **27**, 781–783.

Wright, A. N. 1992 Coupling of fast and Alfvén modes in realistic magnetospheric geometries. *JGR* **97**, 6429–6438.

Zorzan, C. 1989 *Resonant Structures in MHD Systems*, Ph.D. thesis, Monash University.

Captions

Table 1 The lowest few frequencies of the discrete spectrum compared with the WKB formula (3.8). Those frequencies marked with an asterisk lie in the gap between the cusp and Alfvén continua. The others lie above the Alfvén continuum.

Figure 1 Energy in the Barston (normal) modes in the case $k_z = 1$, with $a_1(0) = 1$ and all the other $a_m(0)$, $b_m(0)$, $c_m(0)$, and all the initial velocities, set to zero (case (a)). The crosses ($\times$) indicate eigenfrequencies from the discrete spectrum, and pluses (+) those from the continua. The two thick "line segments" near the bottom left corner represent in fact these two continua, made up in this case of around 120 closely packed pluses. Note the single discrete mode sitting just above the lower (cusp) continuum. Total energy is normalized to unity, here and in all other figures.

Figure 2 Same as figure 1, but for $k_z = 3$ (case (b)). There are now two discrete eigenvalues in the gap between the continua.

Figure 3 Same as figure 1, but for $k_z = 10$ (case (c)). There are now seven discrete eigenvalues in the gap between the continua.

Figure 4 Same as figure 1, but for $k_z = 10$, $a_1(0) = 0$, and $c_0(0) = 1$ (case(d)).

Figure 5 Energy in the Fourier modes at time $t = 400$ in case (a), corresponding to figure 1. The upper panel refers to the total energy, the lower one to that in the continuum only. Initially, all energy is at $m = 1$.

Figure 6 Energy in the Fourier modes at time $t = 125$ in case (b), corresponding to figure 2. Initially, all energy is at $m = 1$.

Figure 7 Energy in the Fourier modes at time $t = 40$ in case (c), corresponding to figure 3. Initially, all energy is at $m = 1$.

Figure 8 Energy in the Fourier modes at time $t = 80$ in case (d), corresponding to figure 4. Initially, all energy is at $m = 0$.

Figure 9 Energy density $H(x, t)$ at time $t = 125$ in case (b). The dashed curves underneath the envelope represent the kinetic, magnetic, and acoustic components of the total energy. Of course, the reader cannot distinguish the details here, but these curves serve to emphasise the fine scales present at the current epoch. The strong peak is due to "resonant absorption" of the "fast wave" manifested as a sharp maximum in energy in the Alfvén continuum in figure 2.

ω_{WKB}	ω for $k_z = 1$	ω for $k_z = 3$	ω for $k_z = 10$
—	—	2.124^*	7.098^*
—	0.723^*	2.148^*	7.124^*
—	1.782	2.308^*	7.172^*
1.343	2.301	4.313	7.257^*
2.686	3.247	4.734	7.399^*
4.029	4.422	5.593	7.633^*
5.372	5.673	6.629	8.018^*
6.715	6.958	7.759	14.163
8.057	8.261	8.948	14.609
9.400	9.576	10.175	15.374
10.743	10.897	11.428	16.225
12.086	12.223	12.699	17.146
13.429	13.552	13.983	18.122
$\vdots$	$\vdots$	$\vdots$	$\vdots$
107.433	107.449	107.504	108.131
$\vdots$	$\vdots$	$\vdots$	$\vdots$

Table 1: The lowest few frequencies of the discrete spectrum compared with the WKB formula (3.8). Those frequencies marked with an asterisk lie in the gap between the cusp and Alfvén continua. The others lie above the Alfvén continuum.

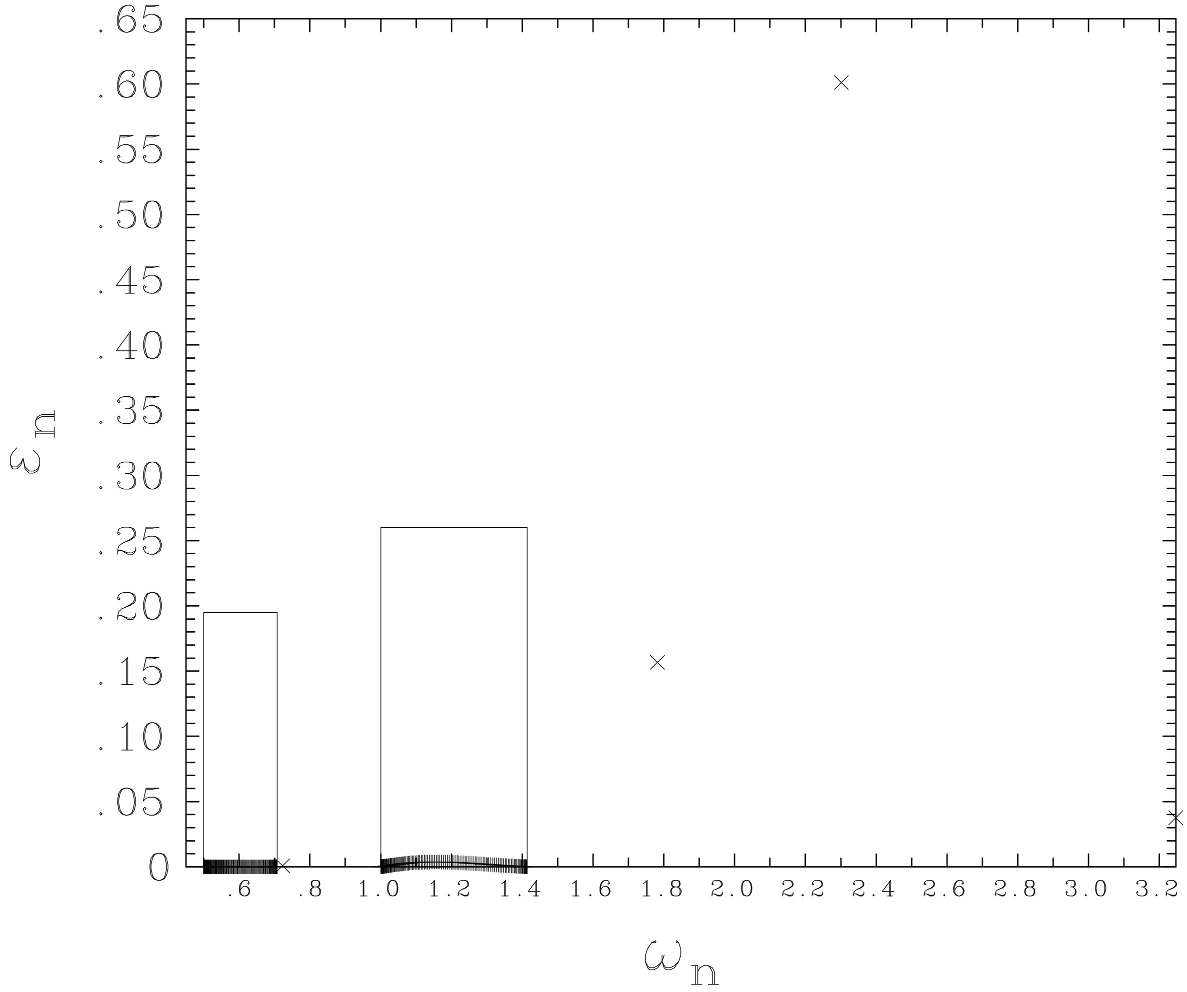

Figure 1: Energy in the Barston (normal) modes in the case $k_z = 1$, with $a_1(0) = 1$ and all the other $a_m(0)$, $b_m(0)$, $c_m(0)$, and all the initial velocities, set to zero (case (a)). The crosses ($\times$) indicate eigenfrequencies from the discrete spectrum, and pluses ($+$) those from the continua. The two thick "line segments" near the bottom left corner represent in fact these two continua, made up in this case of around 120 closely packed pluses. Note the single discrete mode sitting just above the lower (cusp) continuum. Total energy is normalized to unity, here and in all other figures.

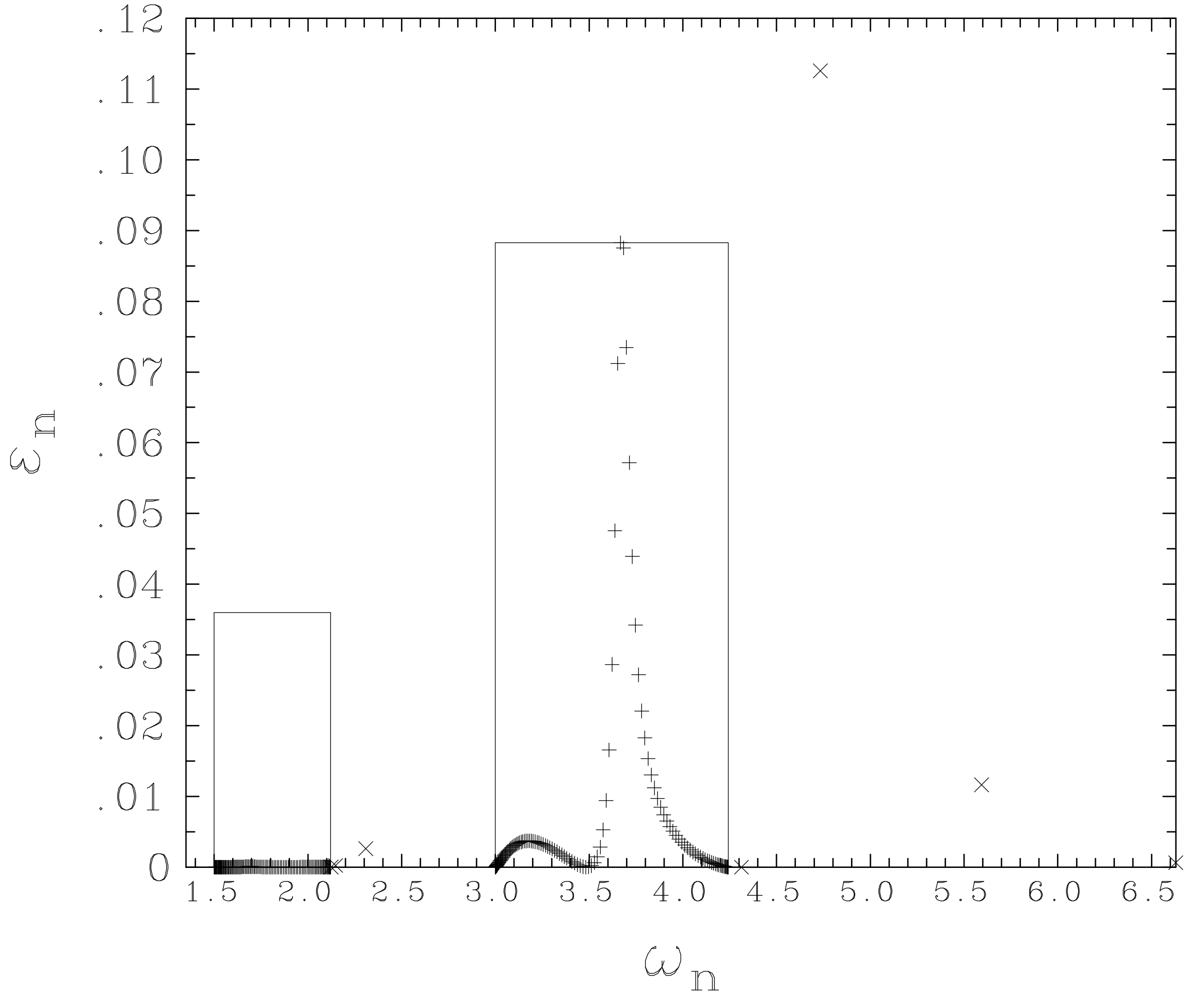

Figure 2: Same as figure 1, but for $k_z = 3$ (case (b)). There are now two discrete eigenvalues in the gap between the continua.

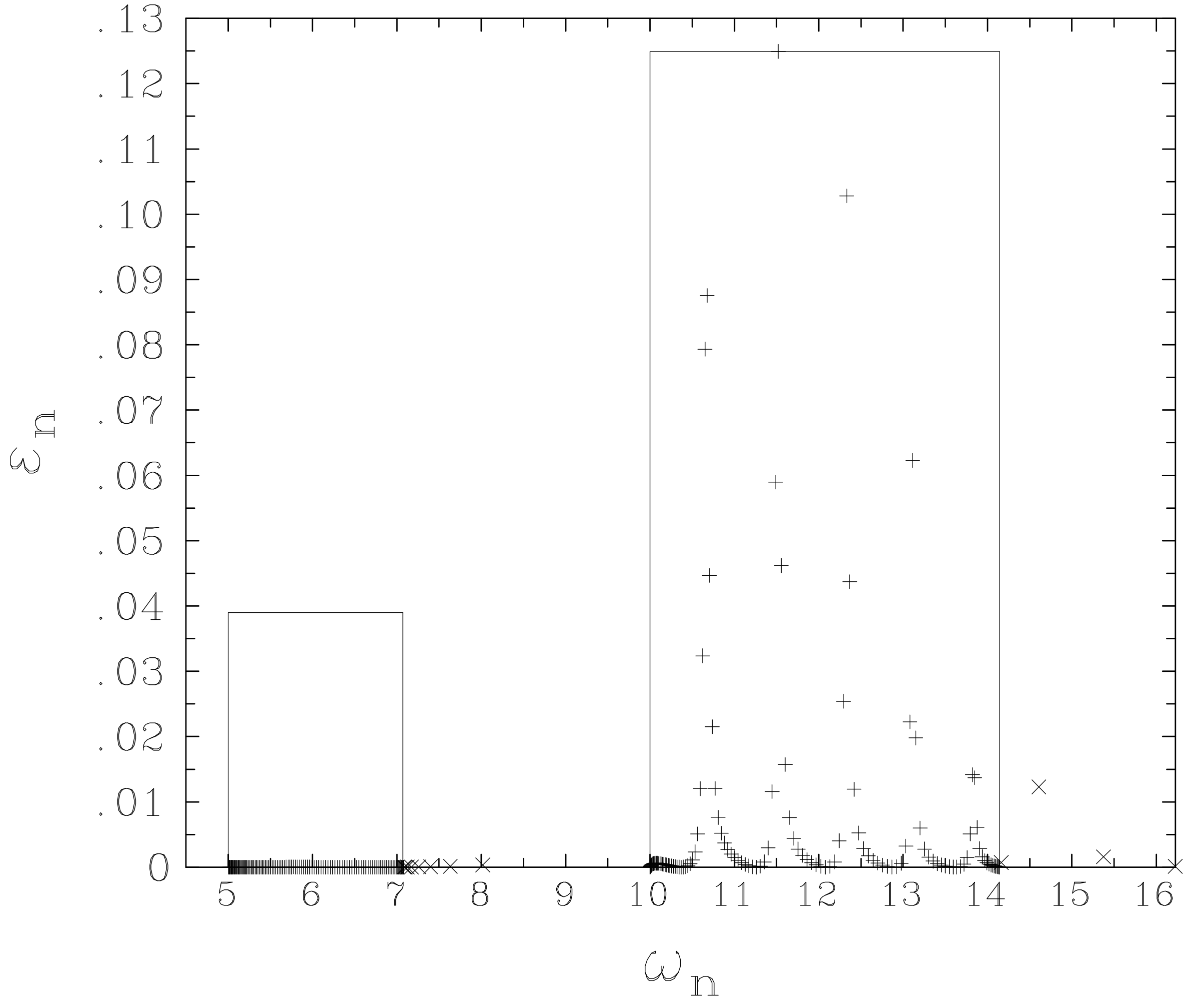

Figure 3: Same as figure 1, but for $k_z = 10$ (case (c)). There are now seven discrete eigenvalues in the gap between the continua.

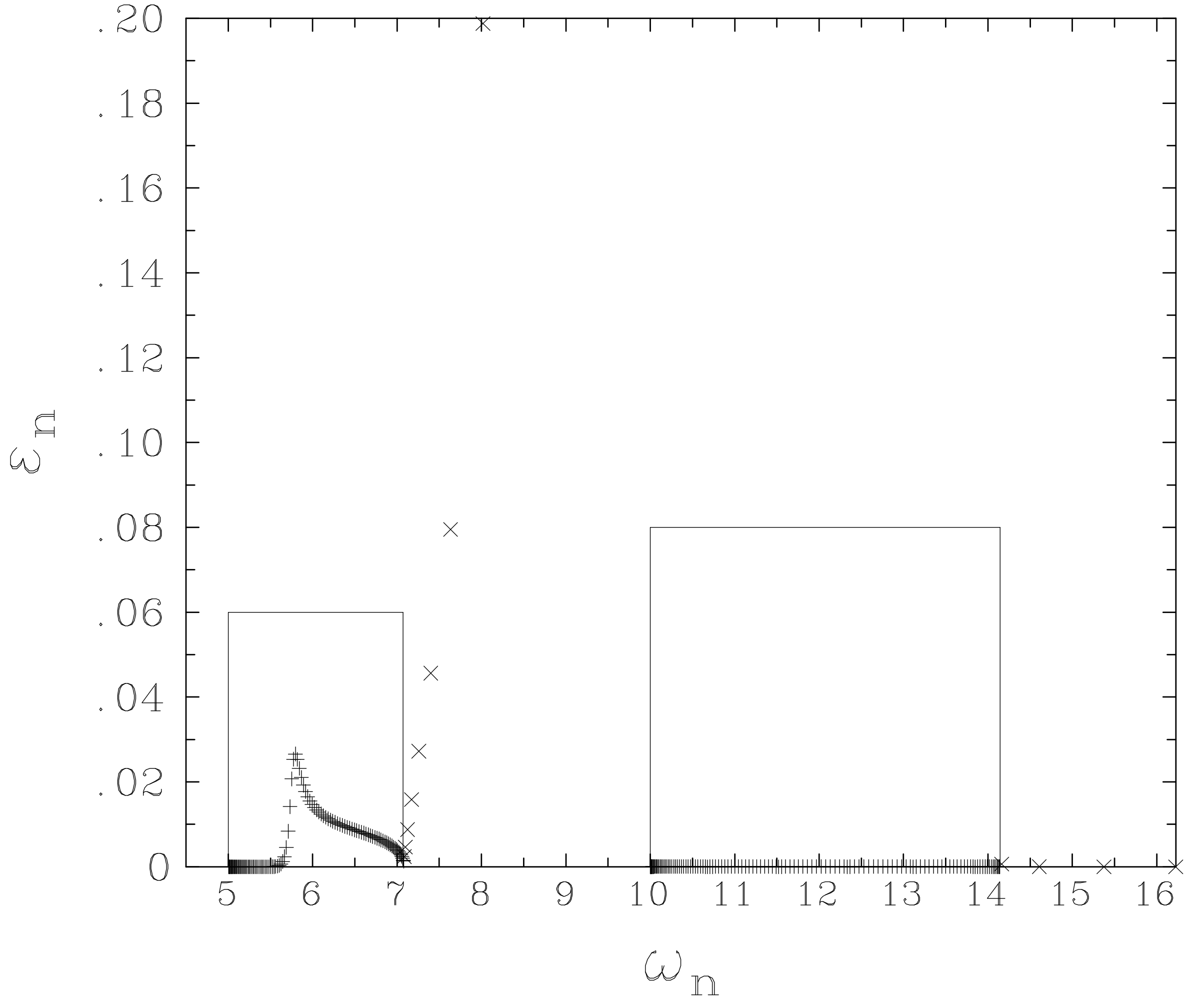

Figure 4: Same as figure 1, but for $k_z = 10$, $a_1(0) = 0$, and $c_0(0) = 1$ (case(d)).

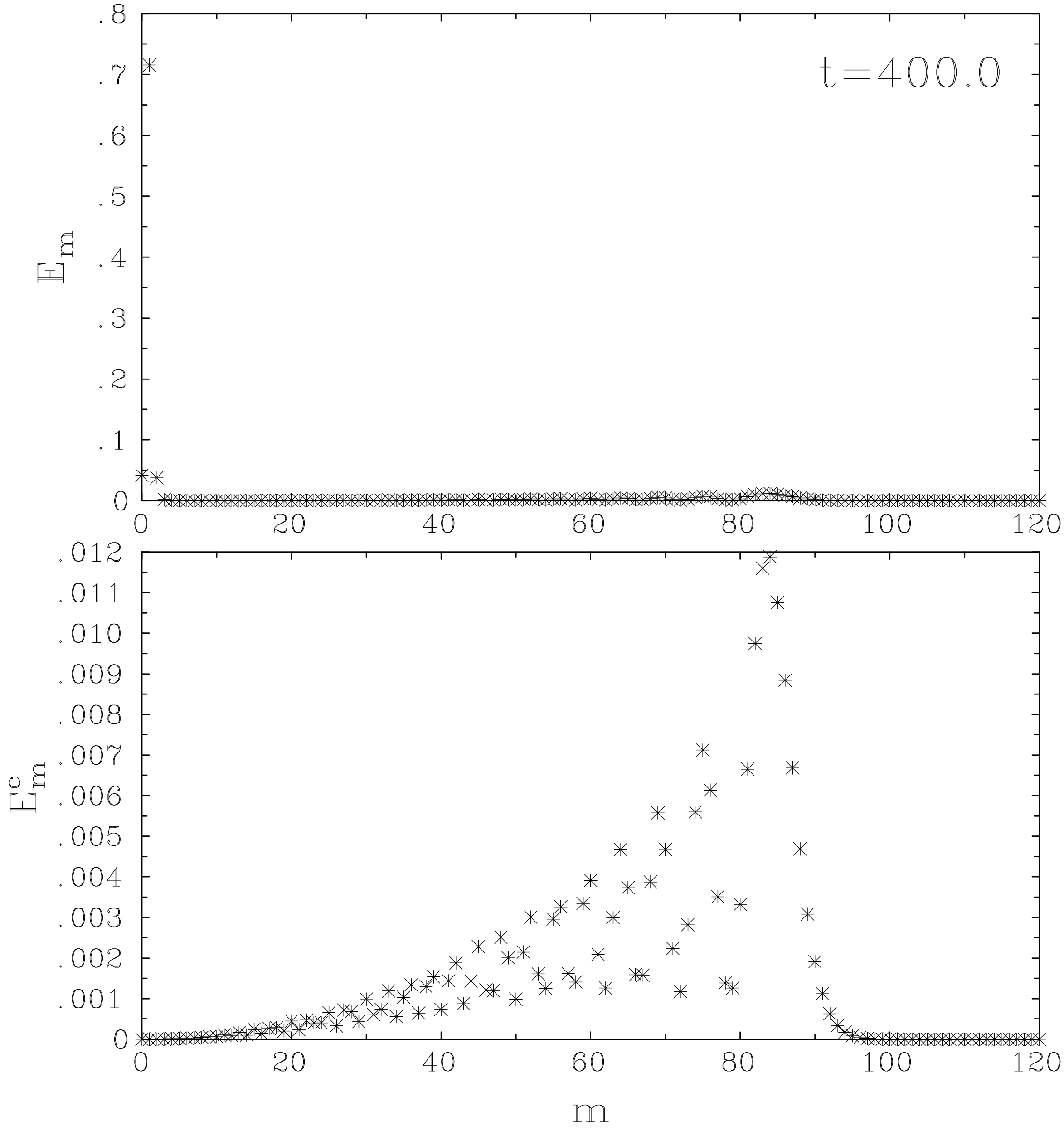

Figure 5: Energy in the Fourier modes at time $t = 400$ in case (a), corresponding to figure 1. The upper panel refers to the total energy, the lower one to that in the continuum only. Initially, all energy is at $m = 1$.

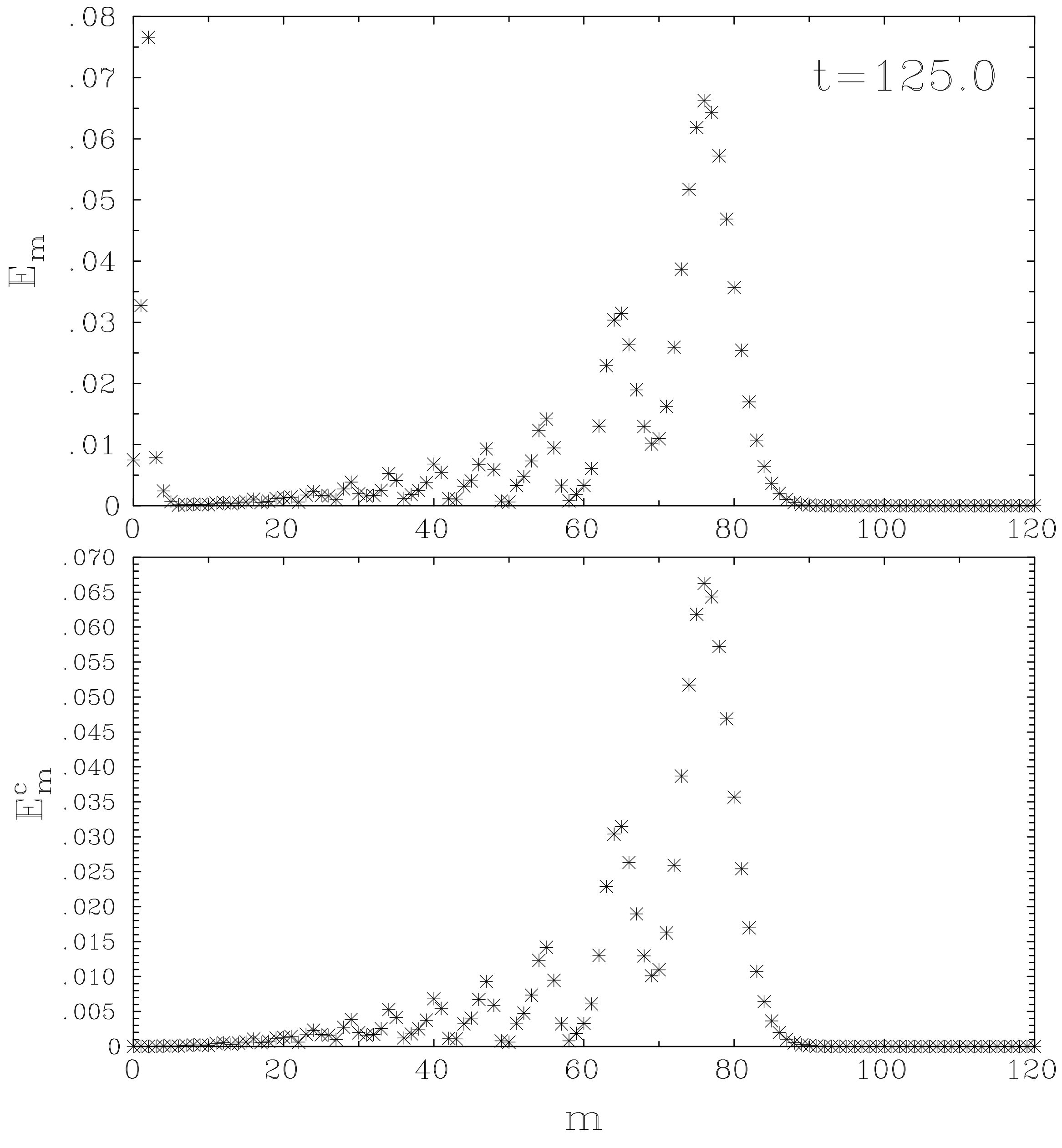

Figure 6: Energy in the Fourier modes at time $t = 125$ in case (b), corresponding to figure 2. Initially, all energy is at $m = 1$.

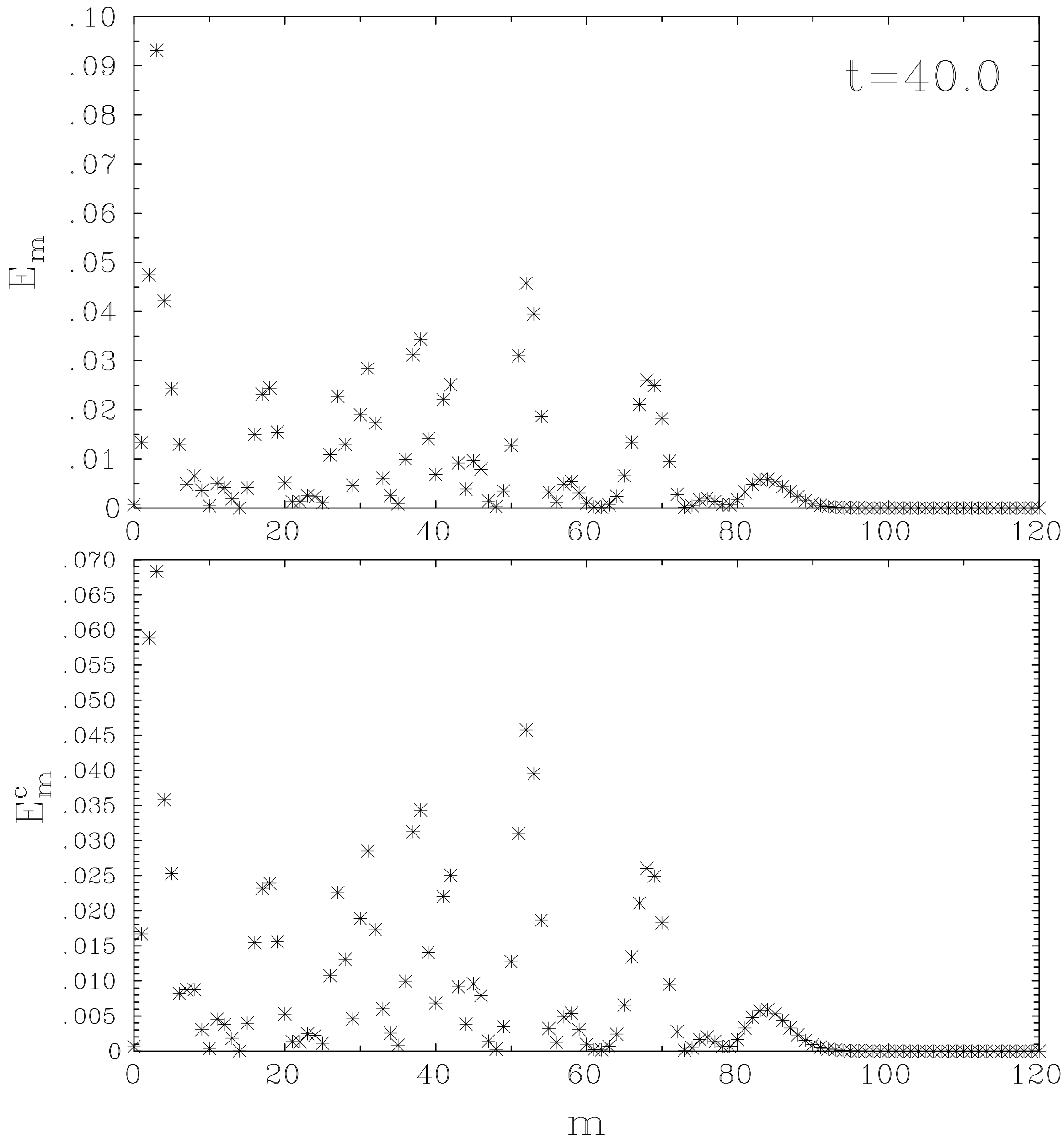

Figure 7: Energy in the Fourier modes at time $t = 40$ in case (c), corresponding to figure 3. Initially, all energy is at $m = 1$.

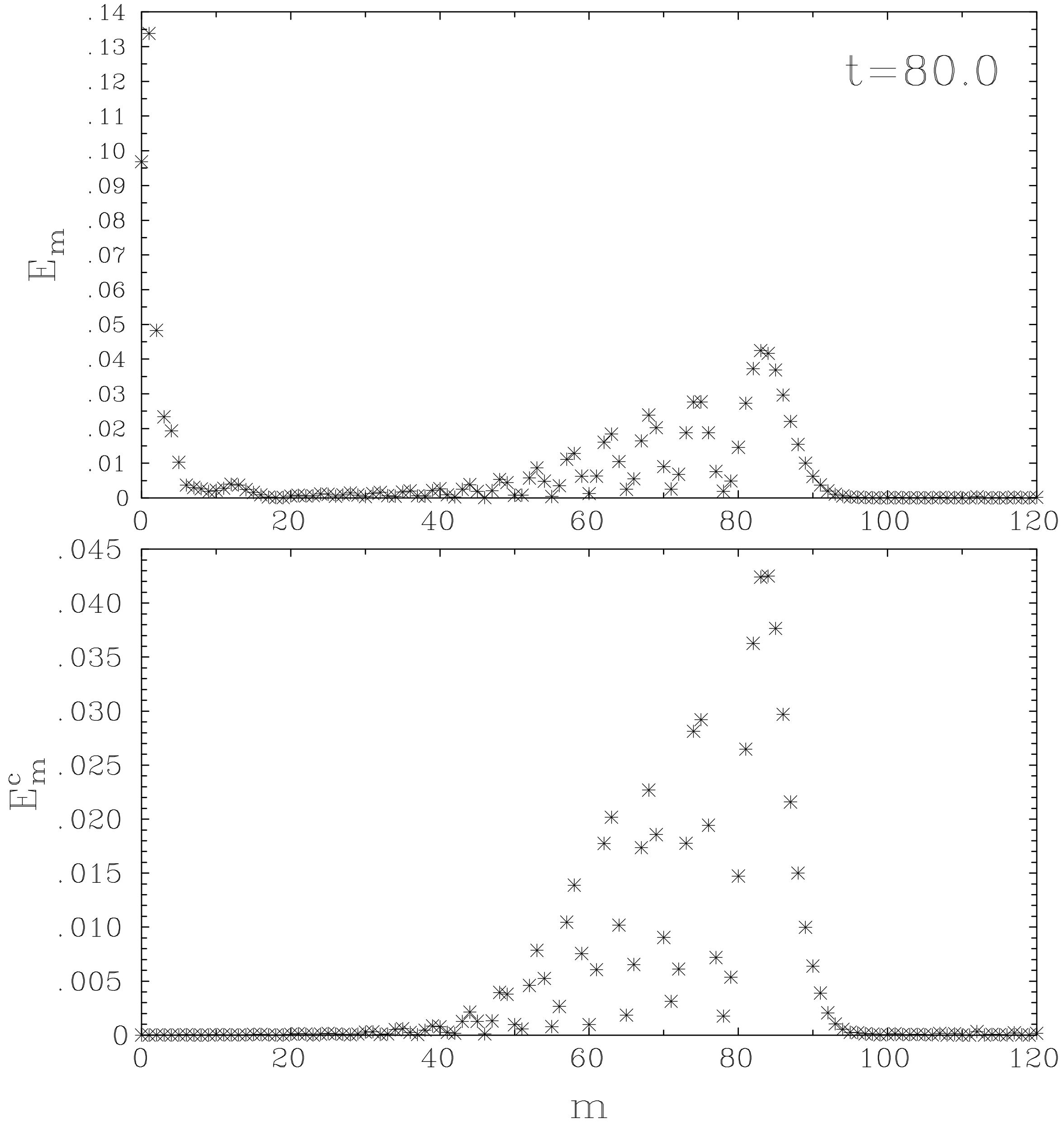

Figure 8: Energy in the Fourier modes at time $t = 80$ in case (d), corresponding to figure 4. Initially, all energy is at $m = 0$.

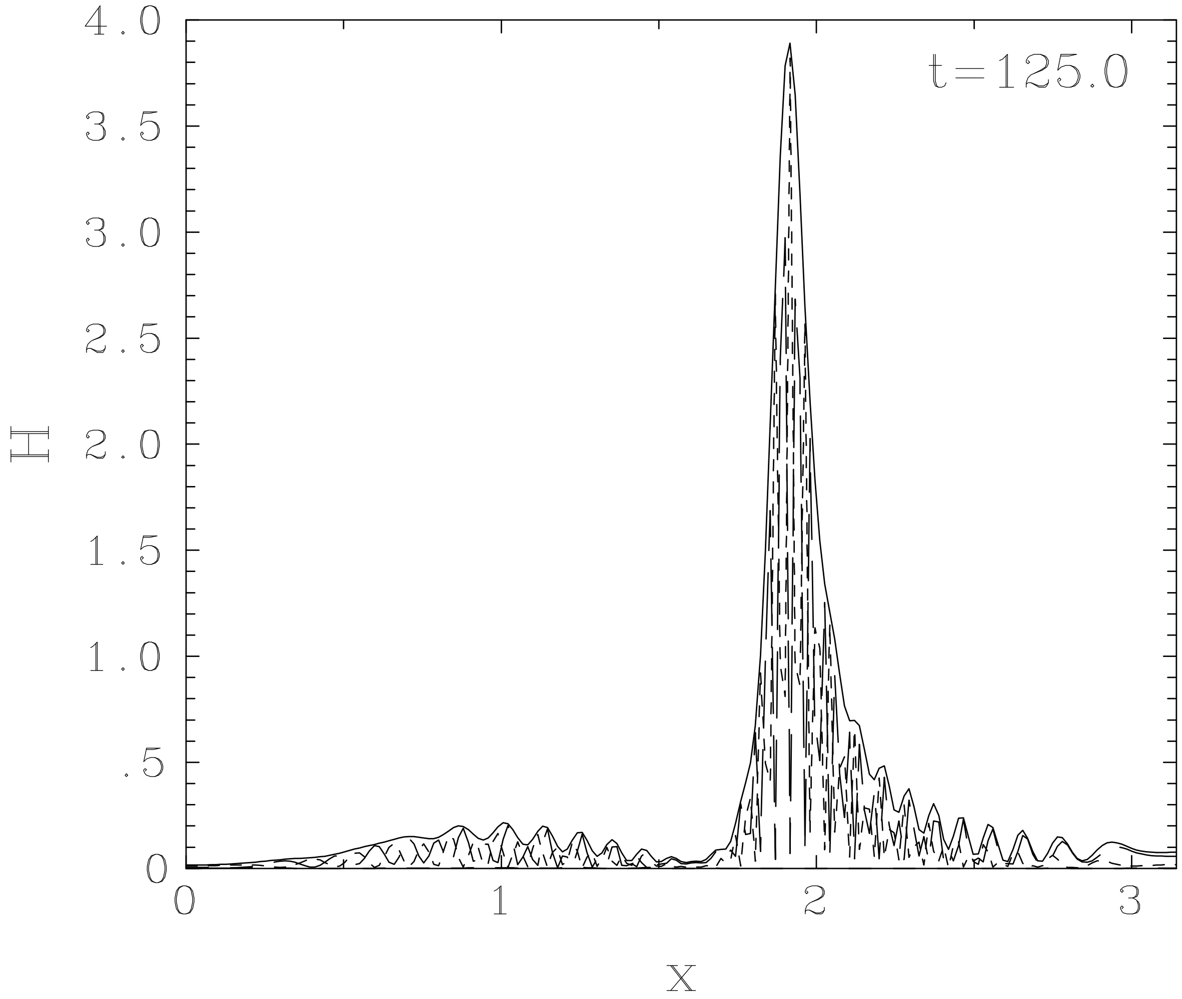

Figure 9: Energy density $H(x,t)$ at time $t = 125$ in case (b). The dashed curves underneath the envelope represent the kinetic, magnetic, and acoustic components of the total energy. Of course, the reader cannot distinguish the details here, but these curves serve to emphasise the fine scales present at the current epoch. The strong peak is due to "resonant absorption" of the "fast wave" manifested as a sharp maximum in energy in the Alfvén continuum in figure 2.